

Received June 18, 2021; reviewed; accepted October 18, 2021

High-temperature carbothermal dephosphorization of Malaysian monazite

Sanjith Udayakumar¹, Sheikh Abdul Rezan Sheikh Abdul Hamid¹, Norlia Baharun¹, Mark I. Pownceby²

¹ School of Materials, Mineral Resources Engineering, Universiti Sains Malaysia, Engineering Campus, Nibong Tebal 14300, Pulau Pinang, Malaysia

² CSIRO Mineral Resources, Private Bag 10, Clayton South, Victoria 3169, Australia

Corresponding author: srsheikh@usm.my (Sheikh Abdul Rezan)

Abstract: High-temperature carbothermal reduction experiments with graphite powder were conducted to assess the dephosphorization behavior of Malaysian monazite concentrate. Thermodynamic analysis of the possible dephosphorization reactions was conducted to evaluate the feasibility of the carbothermal reduction of the monazite phases. The effects of temperature, particle size, and monazite to carbon ratio were then investigated under different conditions. The carbothermal reduction experiments were conducted based on the Taguchi design method, and up to 97% of phosphorous removal was achieved under optimized conditions. The optimal conditions for dephosphorization were determined as; a reduction temperature of 1350 °C, a particle size of -75 µm, and monazite to carbon molar ratio of 0.3. Microstructural and phase characterization of the dephosphorized products revealed that CeO₂, Nd₂O₃, La₂O₃, and Pr₂O₃ oxide phases were prominent, and no residual peaks of monazite remained in the reduced products. The information gained from the study can aid in the design of a suitable post-dephosphorization hydrometallurgical treatment for exploiting Malaysian monazite as a local source of REEs.

Keywords: malaysian monazite concentrate, dephosphorization, carbothermal reduction, rare earth elements, graphite

1. Introduction

Monazite is a rare-earth phosphate group mineral with the general formula (Ce, La, Nd, Th)PO₄ that is commercially extracted from hydrothermal and placer deposits in Malaysia, Thailand, China, India, Australia, Brazil, and some parts of North America. The recovery of monazite is mostly obtained as a by-product of cassiterite mining and from rutile, zircon, and ilmenite-bearing heavy mineral sand deposits. Monazite is a refractory mineral having high thermal stability and exhibiting high resistance to natural weathering processes. The amount of phosphorous in monazite varies from 24.5-30 wt.% depending upon the geological environment in which it formed; however, the primary use for monazite is as a source for light rare earth elements (LREEs) and radioactive species such as thorium and uranium (Krishnamurthy and Gupta, 2015; Nriagu, 1984). The refractory behavior of monazite means that aggressive chemical leach processes are usually applied in the extraction of RE elements; however, the success of these processes depends critically on the properties and mineralogical composition of the monazite concentrate being processed. The current study emphasizes the importance of understanding the mineralogy and chemistry of a monazite concentrate sourced from Malaysia to identify an appropriate process for recovering the contained RE elements.

Existing conventional chemical methods for processing monazite concentrates on extracting RE elements involve either acid leaching or alkaline digestion processes. In the acid leaching process, monazite is reacted with mineral acids such as sulphuric acid, nitric acid, or hydrochloric acid at

elevated temperatures for several hours to decompose ('crack') the phosphate structure. The acid leaching is followed by a series of hydrometallurgical processes for rare earth recovery (Berry et al., 2018; Karshigina et al., 2018). In contrast, the alkaline digestion method is a fusion process that uses caustic soda as the cracking agent for decomposing the monazite at high temperatures (Kumari et al., 2015; Sadri et al., 2017). Apart from the above-mentioned industrially practiced methods, alternative methods of processing monazite for recovering the REEs include high-temperature reduction (Merritt, 1990a; Merritt, 1990b; Kemp and Cilliers, 2016) and roasting (Zheng et al., 2017a; Franken, 1995), mechano-chemical decomposition (Kim et al., 2009), and other unconventional methods (Xing et al., 2010; Berry et al., 2017; Ha, 1979; Huang et al., 2016; Zhang and Lincoln, 1994; Zheng et al., 2017a; Keekan et al., 2017). In most methods proposed for processing monazite, there is a possibility of phosphide (complexes containing the P^{3-} anion) formation which can remain stable in acid or alkaline environments resulting in contamination of the end products and thereby affecting their functionality. Therefore, there is a need to remove phosphorous from monazite by employing pre-treatment processes, usually involving decomposition of the phosphate matrix. The nature of the decomposition process is usually determined by the physical and chemical characteristics of the monazite mineral concentrate, which includes knowledge of the chemistry, mineralogy, and chemical reactivity.

One of the potentially effective ways of decomposing monazite to remove phosphorous is by carbothermal reduction using reductants such as coke, activated carbon, and charcoal. The carbothermal reduction approach combines the reducing properties of carbon with high temperatures to produce a reduction phenomenon in the reacting system. Previous studies have demonstrated that charred coal is an effective reductant to dephosphorize monazite concentrates under high-temperature conditions (Xing et al., 2010). For example, monazite dephosphorization behavior was compared using charred coal and coking coal for mixed RE concentrate from a Baotou, China, wherein charred coal was more effective due to its higher carbon content and lower volatile and ash content (Pengfei et al., 2010). A novel and environment-friendly Coal- $Ca(OH)_2$ -NaOH roasting decomposition approach was used for Bayan Obo RE-containing magnetite tailings by varying the roasting parameters (Zheng et al., 2017b). The findings optimized the process for producing RE elements and oxides in the roast products. Another study investigated the roasting of the Bayan Obo magnetite-rich RE tailings using CaO-Coal, and the decomposition kinetics and phase transformations of the RE elements and oxides were studied (Yuan et al., 2017). Note that for the Bayan Obo deposit, carbon roasting is performed for a different reason, i.e., for the removal of iron. The nature of the ore (Bayan Obo tailings) is Fe-rich; therefore, the carbon-based reduction is necessary for the recovery of Fe, thereby aiding the reduction of the REEs in the subsequent activation roasting.

Although the studies in the literature have demonstrated several forms of carbon to have the capacity to reduce the monazite-rich concentrates to their oxides at high temperatures, a major issue with carbothermal or high-temperature reduction is the formation of RE carbides which may also form solid solutions with oxygen and nitrogen (e.g., oxycarbides and oxycarbonitrides). In order to avoid the possible formation of highly stable carbides, appropriate conditions of temperature, CO/CO₂ molar ratios, and high vacuum need to be chosen. However, there is insufficient experimental data available to construct Pourbaix-Ellingham diagrams for these systems, and as a result, it is challenging to predict and control the reaction (Gupta and Mukherjee, 1990; Kemp, 2017). Moreover, the recovery of phosphate from monazite has not been of significant interest in the past, and the separation of REEs (and/or Th) from the reduced product has not been investigated in detail. These factors have made high-temperature reduction processes for REE recovery from monazite a less preferred option over existing hydrometallurgical methods in commercial usage. Several forms of carbon, such as coke, coal, char, deposited carbon, and activated carbon, can be used for the reduction of monazite. In the current study, graphite was chosen as the reducing agent. Graphite is a pure form of carbon, with a higher amount of fixed carbon and low ash content, which becomes highly crystalline at high temperatures wherein it becomes increasingly reactive and should, therefore, enhance the reducibility of monazite (Suárez-Ruiz and Crelling, 2008). Despite the high temperature required, the process using carbon is highly efficient, repeatable, convenient, and pure graphite is available at a low cost. Pure graphite acts as an effective reducing agent for higher temperatures, especially above 1100°C, compared to coal, coke, and activated carbon (Tripathy et al., 2012; Wang and Yuan, 2006). The graphite particles are very fine,

i.e., high specific surface area, meaning that there would be many contact points and higher surface activity between the mineral and reducing agent, so the kinetics of reduction would be worth investigating. Limited research has been carried out so far using carbon-based reducing agents for processing monazite, and the potential of graphite as a reducing agent in REE production has not been explored.

The effect of graphite as the reducing agent was investigated within a range of parameters, including the reduction temperature, the particle size of the monazite concentrate, and the molar ratio of monazite to graphite. Thermodynamic evaluation of the monazite decomposition/dephosphorization process in both the absence and presence of carbon was used to complement the experimental findings and form the background for designing the experiments and understanding the mechanism of reduction of the REE's. The research will provide a basis for understanding the pyrometallurgical approach using graphite for processing monazite to recover RE elements.

2. Thermodynamic analysis of monazite decomposition

Thermodynamic analysis of the decomposition reaction of the major constituent phases of Malaysian monazite, CePO_4 , LaPO_4 , and NdPO_4 into the oxides Ce_2O_3 , La_2O_3 , and Nd_2O_3 plus a phosphorus-containing compound was performed using Outokumpu HSC v6.0 software (Roine et al., 2006). Note that natural monazite is typically a complex solid solution between all three end-member components; however, no REE-based solid solutions were considered in the thermodynamic analysis due to a lack of data for the solid solution phases. The thermodynamic analysis was conducted for graphite-free and graphite-present conditions.

2.1. Monazite decomposition (graphite-free)

The general reaction of decomposition of monazite in the absence of a reductant is expressed using Eq. (1):



where RE = Ce, La, Nd, Y; X = P_2O_5 , $\text{P}_2\text{O}_5(\text{g})$, $\text{PO}(\text{g})$, $\text{PO}_2(\text{g})$, $\text{P}_4\text{O}_6(\text{g})$, $\text{P}(\text{g})$; y , z indicate stoichiometry. Results for the pure end-member compositions are shown in Fig. 1. The values of ΔG° for CePO_4 indicate decomposition commences between 1500 and 1600 °C, wherein either P_2O_5 or P_4O_6 is formed. In comparison, the decomposition temperatures were found to be significantly higher (up to 2300 °C) for pathways producing $\text{PO}(\text{g})$, $\text{PO}_2(\text{g})$, and $\text{P}(\text{g})$ as products. Both theoretical (Figs. 1b and 1c) and experimental TG-DTA studies (see below) indicate that LaPO_4 and NdPO_4 decompose at relatively higher temperatures than CePO_4 . A diagram contrasting the changes in standard Gibbs's free energy (ΔG°) for the decomposition of the three distinct RE phosphates CePO_4 , LaPO_4 , and NdPO_4 to produce the RE oxide and $\text{P}_2(\text{g})$ is shown in Fig. 2. Results indicated that the decomposition reaction occurs only when temperatures reaches higher than 2100 °C. The dissociation of the RE phosphates to its constituent oxides and $\text{P}_2(\text{g})$ requires a large amount of energy because of the high ionic and crystal lattice strength of monazite (Kemp and Cilliers, 2016). The higher chemical bond strength of the phosphate structure (P-O) can also be attributed to the ability of the crystal lattice to resist thermal decomposition even at elevated temperatures (Cottrell, 1958). The thermodynamic analysis also revealed that different varieties of cerium oxide compounds were formed during the reduction process, which may pose difficulties during subsequent processing as the cerium ions (e.g., Ce^{4+} in CeO_2) exhibit a selectively soluble behavior, resulting in incomplete dissolution when leached even in strong mineral acids (Abreu and Morais, 2010).

2.2. Monazite decomposition (graphite-present)

In the presence of excess carbon, monazite dissociates to produce RE oxides, phosphor gas, and carbon monoxide (Xing et al., 2010). The general reaction for the high-temperature carbothermal dephosphorization of monazite using graphite is given by Eq. (2):



All possible reactions are listed in Table 1, along with the calculated change in Gibbs free energy, ΔG° ,

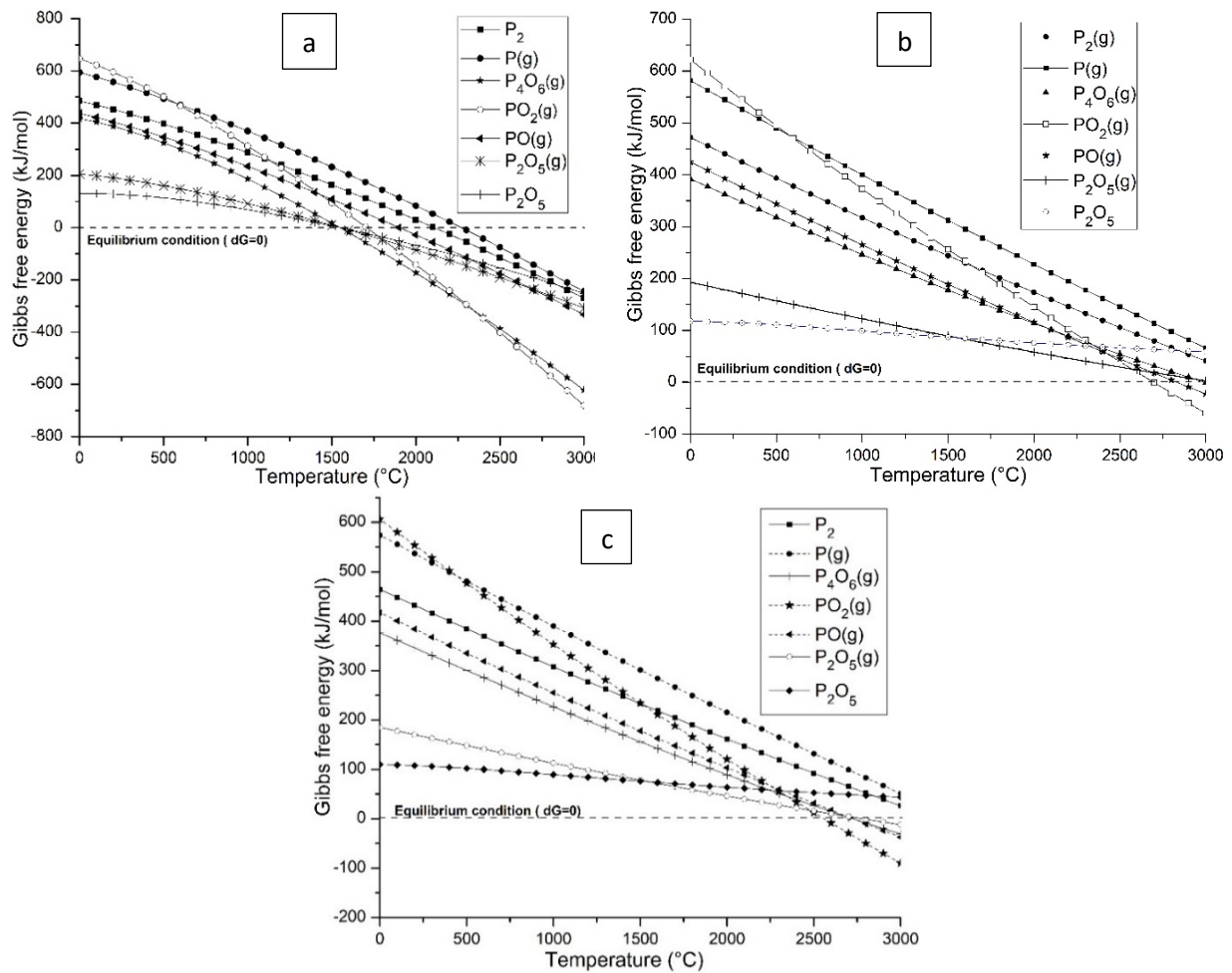


Fig. 1. Reaction feasibility diagrams for the dissociation of: a) CePO_4 into Ce_2O_3 and X, b) LaPO_4 into La_2O_3 and X, and c) NdPO_4 into Nd_2O_3 and X, where, in each case, X = P_2O_5 , $\text{P}_2\text{O}_5(\text{g})$, $\text{PO}(\text{g})$, $\text{PO}_2(\text{g})$, $\text{P}_4\text{O}_6(\text{g})$ and $\text{P}(\text{g})$

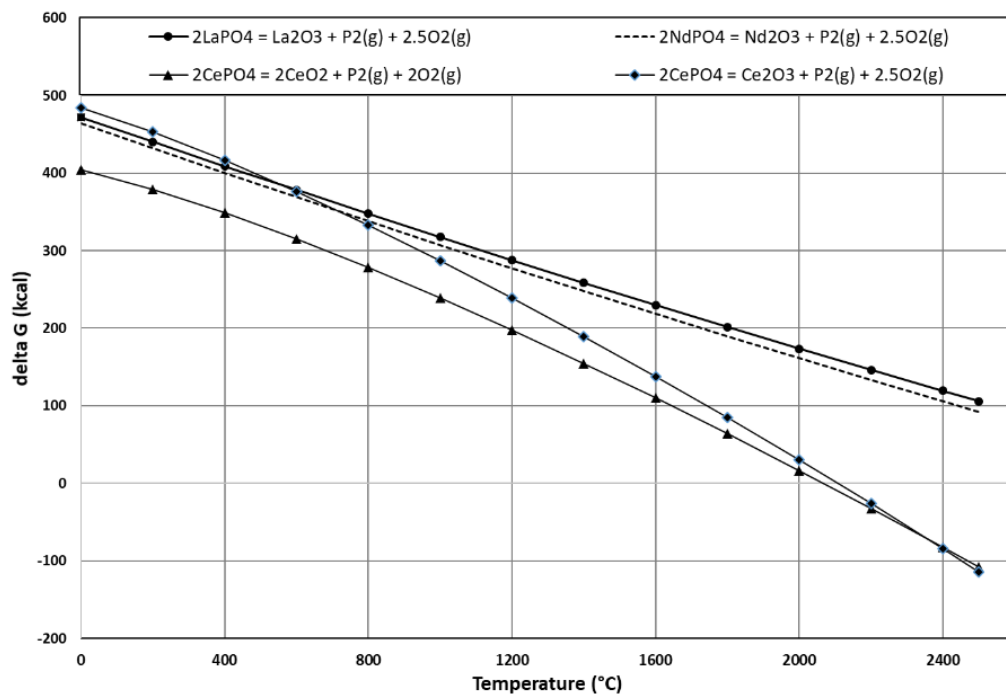


Fig. 2. Gibbs Free Energy diagram for the overall decomposition reactions for different end-member components in monazite (graphite-free)

Table 1. Relationship between Gibbs Free Energy (ΔG° , kJ/mol) and equilibrium temperature (T_{eq} , °C) for possible reactions involving different end-member components of monazite with varying amounts of graphite

Reaction ID	Possible Reactions	ΔG° (kJ/mol)	Equilibrium Temperature T_{eq} (°C)
(a)	$2\text{CePO}_4 + 5\text{C} = \text{Ce}_2\text{O}_3 + \text{P}_2(\text{g}) + 5\text{CO}(\text{g})$	$-1.3437T + 1408$	1048
(b)	$2\text{CePO}_4 + 4\text{C} = 2\text{CeO}_2 + \text{P}_2(\text{g}) + 4\text{CO}(\text{g})$	$-1.1203T + 1208$	1078
(c)	$2\text{CePO}_4 + 12\text{C} = 2\text{CeC}_2 + \text{P}_2(\text{g}) + 8\text{CO}(\text{g})$	$-1.9151T + 2610.9$	1363
(d)	$2\text{CePO}_4 + 11\text{C} = \text{Ce}_2\text{C}_3 + \text{P}_2(\text{g}) + 8\text{CO}(\text{g})$	$-1.9078T + 2545.9$	1334
(e)	$2\text{Ce}_2\text{O}_3 + \text{O}_2(\text{g}) = 4\text{CeO}_2$	$0.2704T - 671.46$	2483
(f)	$4\text{CeO}_2 + \text{C} = 2\text{Ce}_2\text{O}_3 + \text{CO}_2(\text{g})$	$-0.2717T + 276.79$	1019
(g)	$2\text{CePO}_4 + 4.44\text{C} = 2\text{CeO}_{1.78} + 4.44\text{CO}(\text{g}) + \text{P}_2(\text{g})$	$-0.2717T + 276.79$	1021
(h)	$2\text{CePO}_4 + 4.56\text{C} = 2\text{CeO}_{1.72} + 4.56\text{CO}(\text{g}) + \text{P}_2(\text{g})$	$-1.2406T + 1302.4$	1050
(i)	$2\text{CePO}_4 + 4.66\text{C} = 2\text{CeO}_{1.67} + 4.66\text{CO}(\text{g}) + \text{P}_2(\text{g})$	$-1.1102T + 1294.5$	1166
(j)	$2\text{CePO}_4 + 4.38\text{C} = 2\text{CeO}_{1.81} + 4.38\text{CO}(\text{g}) + \text{P}_2(\text{g})$	$-1.0432T + 1224.4$	1174
(k)	$2\text{CePO}_4 + 4.34\text{C} = 2\text{CeO}_{1.83} + 4.34\text{CO}(\text{g}) + \text{P}_2(\text{g})$	$-1.1974T + 1263.9$	1056
(l)	$2\text{CePO}_4 + 2.5\text{C} = \text{Ce}_2\text{O}_3 + 2.5\text{CO}_2(\text{g}) + \text{P}_2(\text{g})$	$-0.9063T + 1099.7$	1213
(m)	$2\text{CePO}_4 + 2\text{C} = 2\text{CeO}_2 + 2\text{CO}_2(\text{g}) + \text{P}_2(\text{g})$	$-0.7704T + 961.33$	1248
(n)	$4\text{CePO}_4 + \text{O}_2(\text{g}) = 4\text{CeO}_2 + 2\text{P}_2\text{O}_5(\text{g})$	$-0.8413T + 1172.1$	1393
(o)	$2\text{LaPO}_4 + 5\text{C} = \text{La}_2\text{O}_3 + 5\text{CO}(\text{g}) + \text{P}_2(\text{g})$	$-1.0768T + 1289.5$	1198
(p)	$2\text{LaPO}_4 + 6\text{C} = 2\text{LaO}(\text{g}) + 6\text{CO}(\text{g}) + \text{P}_2(\text{g})$	$-1.5769T + 2574.5$	1633
(q)	$2\text{LaPO}_4 + 6\text{C} = \text{La}_2\text{O}_2(\text{g}) + 6\text{CO}(\text{g}) + \text{P}_2(\text{g})$	$-1.4091T + 2240.4$	1590
(r)	$2\text{LaPO}_4 + 4\text{C} = 2\text{LaO}_2(\text{g}) + 4\text{CO}(\text{g}) + \text{P}_2(\text{g})$	$-1.275T + 1963$	1540
(s)	$2\text{NdPO}_4 + 5\text{C} = \text{Nd}_2\text{O}_3 + 5\text{CO}(\text{g}) + \text{P}_2(\text{g})$	$-1.0855T + 1256.4$	1157
(t)	$2\text{NdPO}_4 + 6\text{C} = 2\text{NdO}(\text{g}) + 6\text{CO}(\text{g}) + \text{P}_2(\text{g})$	$-1.6018T + 2550.4$	1592

and the equilibrium temperature for each reaction. Note that the equilibrium compositions of the reaction products formed were calculated for different molar ratios of phases of monazite (CePO_4 , Ce_2O_3 , CeO_2 , LaPO_4 , and NdPO_4) to graphite (C). The large negative value of ΔG° with respect to increasing temperature indicates that all reactions will occur only when the temperature is greater than 1000 °C. However, in comparison to heating monazite in air, the results show that when the individual RE phosphates within monazite are heated in the presence of carbon at different carbon to monazite ratios, the dissociation temperature is significantly lowered compared to the carbon-free results.

For example, in the carbon-free system, CePO_4 dissociated to Ce_2O_3 and $\text{P}_2(\text{g})$ at ~2000 °C, whereas in the carbon-present system, results indicate dissociation occurred at temperatures ~1050 °C. Furthermore, the thermodynamic functions calculated for reactions involving Ce-based compounds highlight the relative instability of the Ce-based phosphate phase, which decomposed to its trivalent and tetravalent oxide components at comparatively lower temperatures than NdPO_4 and LaPO_4 monazites. While CePO_4 exhibited lower thermal stability, beginning to decompose around 700 °C, LaPO_4 and NdPO_4 both remained stable up to a range between 1000 and 1400 °C in the reducing environment. The analysis also showed that only oxide species were formed in the specified temperature range, while no oxy-carbides or carbides were present. However, it can be noted that when the ratio of monazite to carbon was increased significantly to about 1:10, i.e., well in excess of the required amount, then Ce-carbides were formed above 1300 °C, whereas La and Nd monazites required higher temperatures and carbon contents to form their corresponding carbides. Although both RE oxides and carbides can be a source of reactive compounds for further RE element recovery processes, both can be treated only using strong mineral acids.

3. Materials and methods

The monazite concentrate was obtained from tin mining tailings from the Ipoh, Perak region of Malaysia. Monazite, a commonly occurring mineral in the heavy tin-tailings called 'Amang,' was

concentrated from the other by-product minerals (xenotime, ilmenite, and zircon) through physical separation methods, namely gravity, magnetic and electrostatic separation and accompanied by flotation process (Jordens et al., 2013). The monazite concentrate comprises small quantities of cassiterite (SnO_2), zircon (ZrSiO_4), quartz (SiO_2), rutile (TiO_2), ilmenite (FeTiO_3), xenotime (YPO_4), Ca-apatite, and K-feldspars (Udayakumar et al., 2020).

3.1. Characterization of Malaysian monazite

Chemical analysis of the bulk monazite concentrate in the form of a fused glass disc was carried out using an XRF spectrometer. The diffraction data of the homogenized sample were collected from $5 - 140^\circ 2\theta$ using a PANalytical Empyrean XRD instrument fitted with a cobalt long-fine-focus X-ray tube operated at 40 kV and 40 mA. Phase identification was performed using PANalytical Highscore Plus© software (V4.5), which interfaces with the International Centre of Diffraction Data (ICDD) PDF4+ database. Rietveld fitting was carried out using TOPAS software (V6). Scanning Electron Microscope (SEM) images were obtained using an FEI Quanta FEG 400 Environmental Scanning electron microscope (ESEM) instrument equipped with a single Bruker XFlash® silicon drift detector for conducting energy-dispersive x-ray spectroscopy (EDX) and Esprit v.1.9 analytical software. Electron Probe Microanalysis (EPMA) to examine the distribution of phases and elements within the monazite concentrate was carried out using a JEOL 8500F microprobe. An area on the polished sample mount was mapped using a combination of wavelength-dispersive and energy-dispersive (ED) spectroscopic techniques. The elements mapped using the WD spectroscopic techniques were Ce, Nd, Th, and La. Elements that were not measured by WD spectroscopy were measured using two energy-dispersive (ED) spectrometers operating in parallel. After mapping, the element distribution data were manipulated using the software package CHIMAGE (Harrowfield et al., 1993), which incorporates an automated clustering algorithm that identifies chemical groupings (Wilson and MacRae, 2005). The clustering procedure used was a multi-element data analysis approach whereby the groupings of elements identified via the clustering algorithm represented statistically different chemical/mineral phases. These phases were then overlaid onto the mapped region to provide a “phase-patched” map showing the distribution of all chemical/mineral phases within the mapped area.

The as-received monazite concentrate was sieved using a sieve shaker apparatus to obtain representative samples for three different size fractions: -75, -125, and -250 μm . The sieved samples were then mixed with different amounts of graphite (<20 μm , Sigma Aldrich) and then composite cylindrical pellets of dimensions 5 mm (h) x 10 mm (diam.) and each weighing about 2 g were prepared. The ideal monazite to carbon stoichiometry was calculated to be 0.4 based on Equation (2) given above, and therefore three different molar ratios (0.3, 0.5, and 0.7) of monazite concentrate to graphite were prepared. Preliminary ‘proof-of-concept’ experiments were conducted at 900 to 1100 $^\circ\text{C}$ to test the procedure and to confirm the dephosphorization temperatures indicated by the thermodynamic analysis. Optimized dephosphorization experiments were then conducted at temperatures ranging from 1250 to 1350 $^\circ\text{C}$ in a horizontal Lenton tube furnace at a heating rate of 10 $^\circ\text{C}/\text{min}$. The ends of the tube were exposed to the atmosphere to allow the CO gas formed during reduction to escape. In this study, time was not considered as an experimental variable, and an experimental run time of 2 h was selected based on previous work of Xing et al. (2010). Gravimetric analysis of the samples was performed before and after dephosphorization to determine the percent weight difference. Morphological and phase analysis of the reduced roast products was also conducted. The extent of dephosphorization was determined based on the phosphorous content for the samples measured by XRF analysis before and after dephosphorization. The percent dephosphorization (D_p) was calculated based on the formula: $(P_i - P_f / P_i) * 100$; where P_i and P_f are the amounts of the phosphorous present in the concentrate before and after the reaction, respectively.

3.2. Optimization of dephosphorization behaviour

The Taguchi experimental design was selected to determine the optimum process parameters and their levels for obtaining the greatest extent of dephosphorization (Taguchi, 1986). Based on the review of existing literature, the thermodynamic analysis, and preliminary test experiments (see below), the following three parameters were expected to have a significant effect on the dephosphorization; (A)

temperature, (B) particle size, (C) molar ratio of monazite to graphite. As indicated above, the experimental run time was kept constant at 2 hrs. For the three factors, three different levels were considered for optimization, as shown in Table 2. Response variables are the experimental outcomes measured in the Taguchi model. As the present study involved the removal of the phosphorous content from the monazite concentrate, a weight loss was observed, and therefore gravimetric change can potentially be used as the response variable. However, a weight loss was also associated with the removal of carbon as CO gas and from any volatile impurities present in the unroasted sample. Thus, the change in overall phosphorous content (i.e., degree of dephosphorization) was the most appropriate response variable to be used in this study. The individual effects of the parameters at different levels on the experimental response were studied by comparing the means of S/N ratios of different experiments.

Table 2. Experimental parameters and their levels

Experimental Parameters	Units	Levels			Response Variable (Y)
		1	2	3	
Reduction Temperature	°C	1250	1300	1350	Degree of Dephosphorization, D_p
Particle Size	µm	-75	-125	-250	
Molar ratio of monazite to graphite	-	0.3	0.5	0.7	

4. Results and discussion

4.1. Characterization of Malaysian monazite

Monazite concentrates commonly contain 24.0-29.0 wt.% of phosphate (P_2O_5), 55.0-60.0 wt.% rare earth metal oxides, 5.0-10.0% thorium oxide (ThO_2) and 0.2-0.4 wt.% uranium oxide (U_3O_8) (Gupta and Mukherjee, 1990). Results from the bulk chemistry determination for the Malaysian monazite sample are provided in Table 3. The data indicates a comparable composition to previous results obtained by Ariffin (2009) for a similar sample from the same source region (Ariffin, 2009). The results in Table 3 indicate the monazite was relatively pure with a composition dominated by the 'light' rare earth element oxides in order of abundance: CeO_2 (36.5 wt.%); Nd_2O_3 (16.5 wt.%); La_2O_3 (13.47 wt.%); Pr_6O_{11} (5.60 wt.%), Sm_2O_3 (2.74 wt.%) and Gd_2O_3 (1.89 wt.%). The ThO_2 content was also high (6.58 wt.%), consistent with monazite, also being a source for thorium. Minor impurities were also present in the sample. These included: SiO_2 (2.05 wt.%) and ZrO_2 (1.18 wt.%), suggesting the possible presence of trace to minor zircon. The elevated Y_2O_3 level (2.11 wt.%) indicated the likely presence of xenotime, which is the iso-structural equivalent of monazite. Other impurities such as TiO_2 (0.367 wt.%), Fe_2O_3 (0.443 wt.%) could indicate the presence of trace ilmenite, whereas CaO (0.923 wt.%) and WO_3 (0.479 wt.%) may indicate scheelite. Clay coatings on particles may be partially responsible for the Al_2O_3 content of 0.246 wt.%.

Table 3. XRF analysis results for the Malaysian monazite (wt.% of constituent oxides)

SiO₂	TiO₂	Al₂O₃	Fe₂O₃	MnO	CaO	P₂O₅	CuO	PbO	WO₃	Nd₂O₃	Pr₆O₁₁
2.05	0.367	0.246	0.443	0.077	0.923	27.27	0.05	0.162	0.479	17.26	2.84
Y₂O₃	ThO₂	U₃O₈	CeO₂	Dy₂O₃	Er₂O₃	Gd₂O₃	La₂O₃	SnO₂	ZrO₂	Sm₂O₃	Tb₄O₇
2.11	6.58	0.342	36.48	0.574	0.137	1.38	13.37	0.406	1.18	2.17	0.118

The quantitative XRD results indicated that the sample contained mainly monazite (>99%). If other impurity phases were present, they were likely at levels below ~1 wt.%. Fig. 3 shows the XRD output from Rietveld modeling, showing the fit of the model to the observed data. Included in the model were Ce, La, and Nd monazite phases. The crystal structure information in Ni et al. was used for the Ce, La, and Nd monazite end-member phases (Ni et al., 1995). An examination of the monazite concentrate using SEM confirmed that the material comprised predominantly single-phase monazite grains. Some monazite grains contained small (5-10 micron) inclusions of phases, including ilmenite, zircon, thorianite, xenotime, and apatite. Discrete gangue mineral phases were also observed in the sample in

trace amounts. These included: zircon, ilmenite, an unidentified Ta/Nb/Fe/Ti phase, cassiterite, scheelite, and wolframite. Representative backscattered electron (BSE) images of the sample and individual monazite and gangue mineral grains are shown in Fig. 4. Examination of a three-color element map produced from EPMA mapping of the concentrate showing the distribution of Ce, P, and Th (Fig. 5a), revealed that all monazite particles were complexly zoned. Chemical clustering of the entire dataset indicated that the sample contained several chemically distinct phases – many of these, however, were single particles of tiny size and small areal extent. In Fig. 5b, the phase-patched map for all phases with an area >1% is shown. Modal analysis results (as an area percent of the mapped area shown in Fig. 5) showed that monazite (96.0%) was the dominant phase, followed by zircon (1.4%), xenotime (0.6%), thorite (0.4%), and cassiterite (0.2%). Trace amounts of quartz, illite, wolframite, and scheelite were also present.

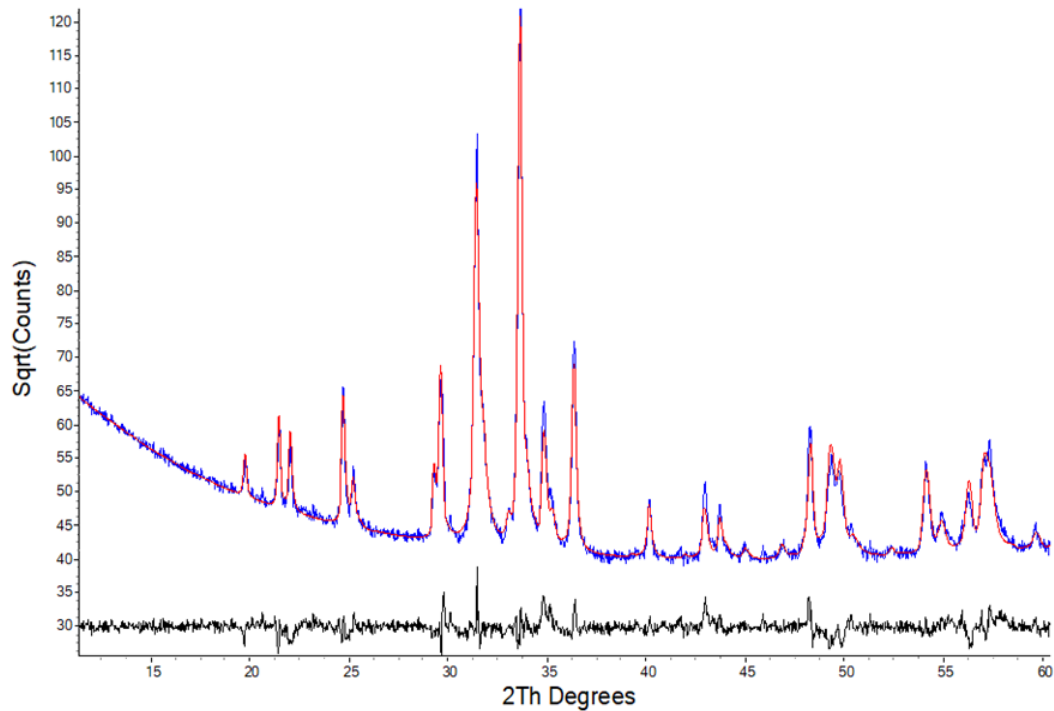


Fig. 3. Rietveld fit to the XRD dataset collected for the monazite sample. The observed data is the solid blue line; the calculated pattern is the solid red line, and the difference pattern is denoted by the black line below

Thermogravimetric and differential thermal analysis (TGA-DTA) was carried out for the raw Malaysian monazite concentrate in the ambient atmosphere until 1100 °C. The monazite concentrate lost approximately 1.1% weight over the temperature range 100-600 °C. The DTA curve exhibited a broad exotherm in the beginning and continued as a broad endotherm between 900-1100 °C. This alternating profile of DTA can be related to two phenomena occurring at the same time of heating, namely, the dehydration of the moisture content in the sample, usually the water of crystallization, and the simultaneous crystallization of the residual amorphous phosphate phases in the mineral. A gradual increase in weight at around 900 °C could be ascribed to the oxidation of the ferrous impurities in the concentrate. The TGA-DTA analysis for a mixture of monazite with carbon (stoichiometric condition of monazite: carbon = 0.4) was carried out to study the decomposition of the phosphate using graphite as a reducing agent (Fig. 6). The thermal stability of the samples was studied for a soaking temperature of 1200 °C for 2 hours after initially heating the sample at a rate of 10 °C/min. An initial broad exotherm in the DTA curve between 150 °C and 450 °C, associated with a weight loss of 2-3 %, was present as in the graphite-free test. This could be due to the crystallization of the residual impurity and amorphous phases in the weathered mineral coupled with the removal of moisture. As a result, a periodic trend was observed until 600 °C with a constant derivative of weight change. Above 600 °C, a very gradual increase in the weight was observed, which might be due to the oxidation of the ferrous impurities present in the sample. Although natural monazite is a thermally stable mineral under high-

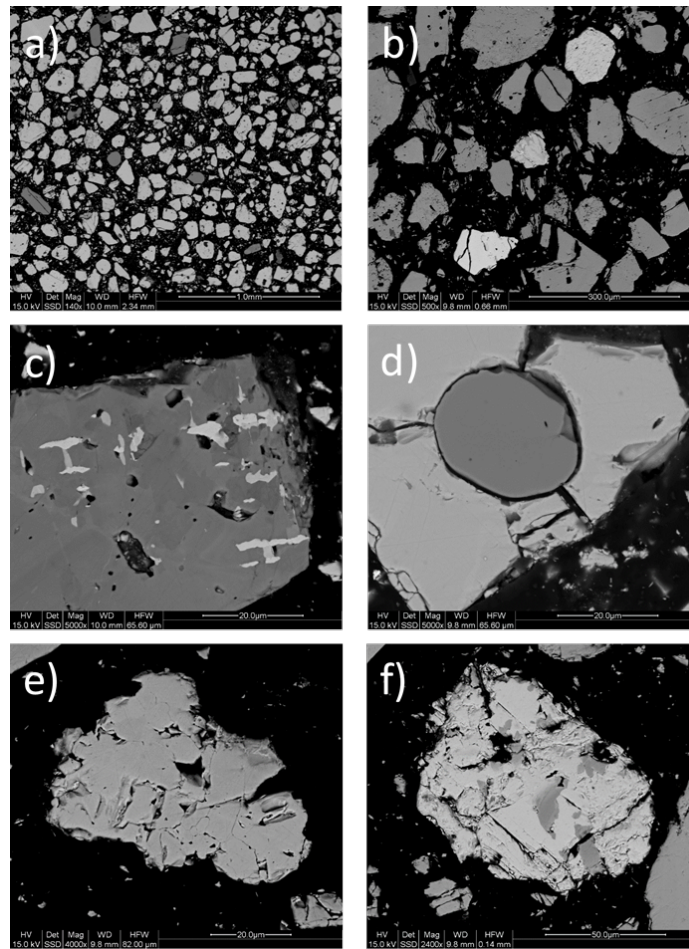


Fig. 4. BSE images for the monazite sample. a) low magnification image showing the sample is mainly monazite (bright phase); however, there are occasional discrete gangue mineral grains (darker) also present, b) three bright contrast gangue grains composed of two columbite grains (bottom left and center) and one scheelite grain (top right), c) a monazite grain containing cassiterite (bright inclusion) and an unidentified Ta/Nb/Fe/Ti phase (medium grey), d) a zircon inclusion in monazite, e) a cassiterite grain, f) a wolframite grain

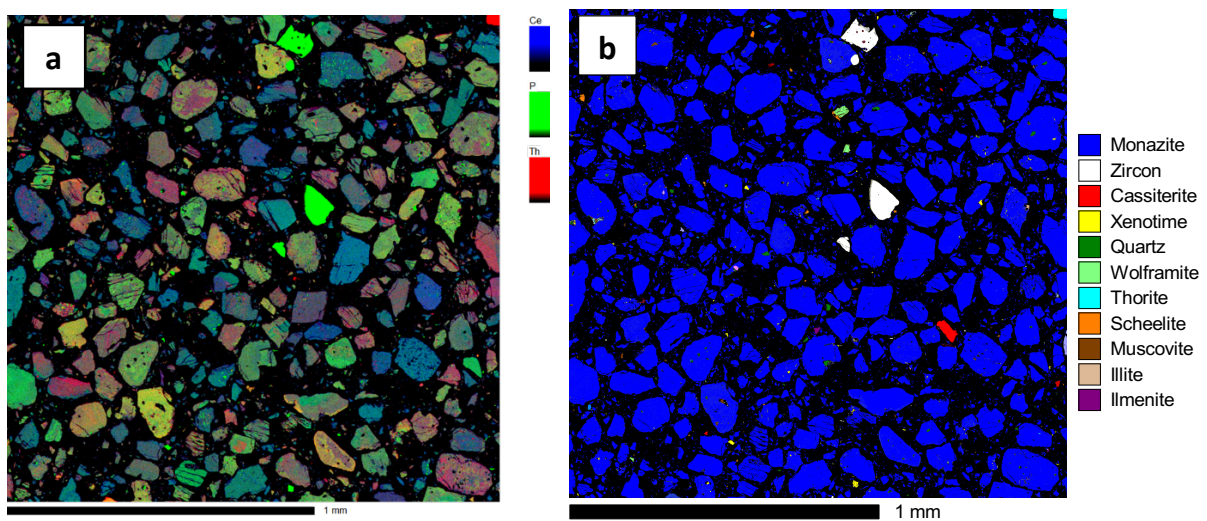


Fig. 5. EPMA map results for the monazite sample showing a) three-color element map showing the distribution of Ce, P, and Th, and b) a phase-patched map showing the types and distribution of mineral phases present. Only phases with an area percent >0.1% are shown

temperature conditions with its high melting point (above 2000 °C), the excess carbon available for reducing the monazite tends to decompose the phosphate structure at a lower temperature – as predicted by the thermodynamic analysis. At 950 °C, a sharp exothermic peak related to a weight loss of 65wt.% was witnessed. A sudden spike in the derivative of weight change was also observed at the same point. The overall trend of the thermogravimetric curve is consistent with a typical decomposition process producing gaseous reaction products, which can be compared to the dephosphorization reaction of monazite wherein carbon monoxide, and phosphorous gases are released. Thus, the DTA curve shows that the breakdown of the monazite concentrate begins at about 950 °C, and the end of breakdown is characterized by a gradual weight gain indicating the formation of rare earth oxides.

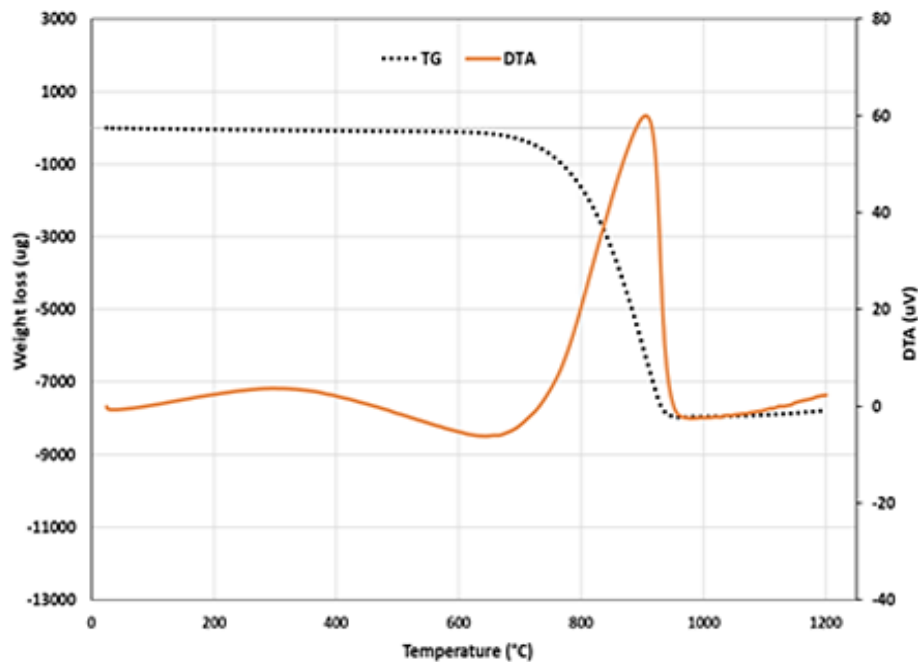


Fig. 6. TG-DTA analysis results from the dephosphorization reaction between monazite with graphite (stoichiometric ratio of monazite: carbon = 0.4)

4.2. Preliminary dephosphorization tests

Five preliminary experiments were conducted based on a small factorial design for examining lower temperatures, namely 900, 1000, and 1100 °C. Thermodynamic predictions indicated that monazite should still be stable under these conditions, and the lower temperature experiments were conducted to check the model calculations. The duration of reduction and particle size of the graphite powder was 2 hours and 75 µm, using monazite: carbon ratios of 0.3, 0.5, and 0.7. The extent of dephosphorization was evaluated based on the weight loss of the reduced samples. Fig. 7 presents the weight loss results observed for the low-temperature dephosphorization experiments. For all temperature conditions, the weight loss was slight but increased slightly with temperature. Similarly, weight loss was influenced by the monazite: carbon ratio, with lowering of the ratio accelerating the dephosphorization process. The weight loss results for the different conditions were in line with the inferences from the thermodynamic and thermogravimetric analysis, which indicated that effective dephosphorization begins to occur at temperatures above about 1200 °C (although note that the DTA results suggested some decomposition occurred beginning around 950 °C consistent with the slight weight loss changes occurring between runs at 900 and 1100 °C). However, it should be noted that while an increase in the reduction temperature promotes dephosphorization of the phosphate mineral, the operating temperature will still be limited to 1350 °C and below, as the thermodynamic calculations indicate potential formation of lanthanide carbides at higher temperatures.

4.3. Optimized dephosphorization tests

The results from the preliminary low-temperature exploratory experiments confirmed that tempera-

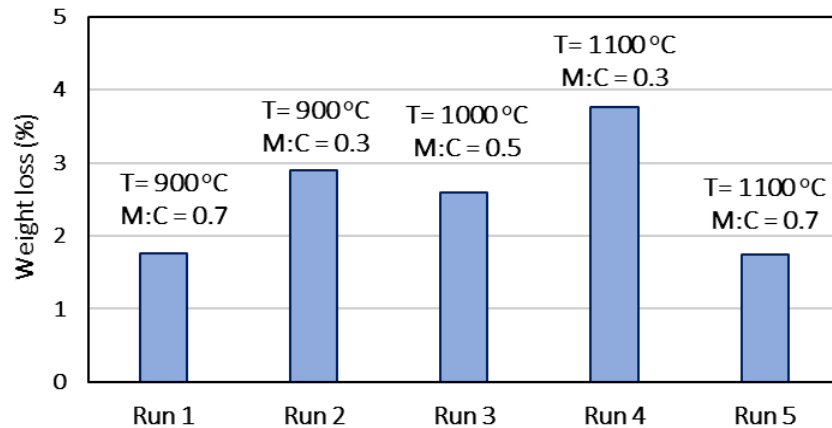


Fig. 7. Weight loss analysis of low-temperature dephosphorization experiments; M:C indicates monazite/carbon ratio

tures >1100 °C and within the range of 1200 to 1350 °C (based on the thermodynamic calculations) were most suitable for dephosphorization under reducing conditions. Using these temperature conditions, additional experiments were conducted with the additional variable parameters of grain size and monazite: carbon ratio according to the Taguchi design matrix in Table 2. Table 4 shows the experimental results for the optimized dephosphorization experiments and their corresponding S/N ratio. The samples were dephosphorized to the extent of 97 % irrespective of the level of the parameters, namely reduction temperature, the molar ratio of monazite to graphite, and the size of the monazite particles. The results show that the decomposition reaction remained relatively insensitive to other parameters such as molar ratio and average particle size once a critical temperature has been reached. The results also indicated that a run time of 2 h was sufficient to induce almost complete dephosphorization, although we note that there is still room for optimization of the time held at that particular temperature.

The Taguchi method utilizes the signal-to-noise ratio (S/N) calculated from the experimental results as an attribute for evaluating the optimal parameter condition. The main effects plot shown in Fig. 8a gives the optimal experimental conditions within the scope of the current study for maximizing the degree of dephosphorization where the more horizontal is the line for a given range of parameters, the less significant is its effect on the dephosphorization. According to the analysis, the monazite to carbon ratio has the most dominant effect, whereas the temperature and particle size have a relatively lower effect on the dephosphorization of monazite. Fig. 8b shows the interaction plot for all parameters examined in this study. Mutual interaction among all parameters is noticeable, with the most notable interference between temperature and the molar ratio. Practically, the increase in temperature and the excess reducing agent will increase the partial pressure of C and at higher temperatures, as the volume ratio of the CO to P₂ produced will be larger than the stoichiometric volume ratio of 5:1. Also, the impurities in the concentrate will produce reduction gases to the gaseous product mixture, subsequently favoring dephosphorization to occur at higher rates at lower temperatures than the actual dissociation temperature of the minerals in the concentrate (Xing et al., 2010). Although lowering the particle size increases the dephosphorization rate, its effect is less extensive than the other two parameters.

Therefore, based on the analysis of the main effects and interaction plots, the optimal parameter levels for monazite dephosphorization in the presence of graphite are a reduction temperature of 1350 °C, a molar ratio of monazite to graphite of 0.3, and a concentrate particle size of 75 μm. An optimized experiment (HTD Best) using these parameters was run and resulted in a dephosphorization percent of 97.86 %, which was comparatively higher than all the other experimental runs in the design.

4.4. Microstructural and phase characterization analysis of the dephosphorized products

The dephosphorized products from the nine experiments plus the optimized experiment were characterized for microstructural and phase analysis using SEM, FTIR, XRD, and EPMA techniques.

Table 4. Taguchi L9 (3³) experimental design, parameters, and results

Run	Sample ID	Temperature (°C)	Particle size (µm)	Molar ratio (Monazite to Graphite)	Degree of weight change (%)	Degree of dephosphorization, n, D _p (%)	S/N Ratio
1	HTD 1	1250	75	0.3	75.61	97.1742	7.9502
2	HTD 2	1250	125	0.5	62.88	97.1892	7.9505
3	HTD 3	1250	250	0.7	58.75	97.0912	7.9487
4	HTD 4	1300	75	0.5	65.94	97.2054	7.9508
5	HTD 5	1300	125	0.7	55.41	97.1048	7.9490
6	HTD 6	1300	250	0.3	74.34	97.1852	7.9504
7	HTD 7	1350	75	0.7	61.82	97.2548	7.9516
8	HTD 8	1350	125	0.3	75.44	97.8501	7.9622
9	HTD 9	1350	250	0.5	58.40	97.3224	7.9529

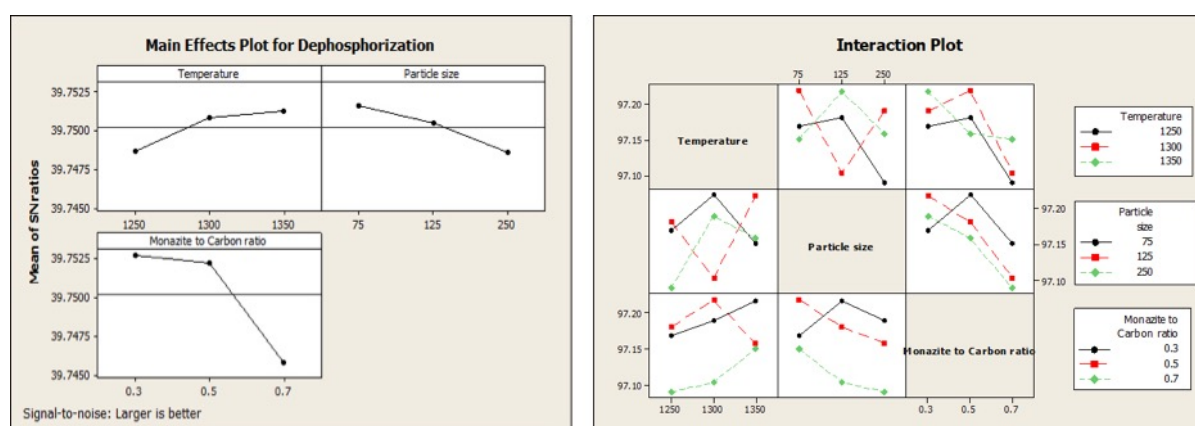


Fig. 8. (a) Main effects and (b) interaction effect plots for monazite dephosphorization

On visual inspection, after dephosphorization, the pellets were slightly deformed at higher temperatures. There was a notable loss in weight, but the solid volume remained largely unaffected. Figs. 9a and 9b show typical changes in the morphology of the mixtures before and after dephosphorization. The surface morphology of the monazite-graphite mixture before heating comprised irregular flaky structures of graphite and minor agglomerations of monazite (Fig. 9a). Since the molar concentration of graphite was in excess of the monazite present in the mixture, the flakes occupy almost 95% of the image. Fig. 9b shows a porous mass of rare earth oxides devoid of graphite flakes in their structure. The granular mass was highly porous due to the removal of P₂ as gaseous products from the monazite structure.

The FTIR spectra for the different dephosphorized samples are presented in Fig. 10. Although only slight differences were observed in the spectral bands between 450-680 cm⁻¹, the transmittance peaks became more prominent and sharper in the dephosphorized samples, which indicated the formation of rare earth oxides. A clear inflection was observed at 950-1150 cm⁻¹ due to the breakdown of the phosphate to oxides. The bands of major rare earth oxides of monazite (Ce, La, and Nd) show similarities to the transmitted spectra of metal oxides studied by Sheibley and Fowler (1966). Fig. 11 shows the XRD patterns of the dephosphorized pellets obtained for three different conditions; HTD 8 (highest degree of dephosphorization), HTD 3 (lowest degree of dephosphorization), HTD Best (Optimal condition) compared to that of the raw monazite concentrate. Peaks corresponding to monazite were not present in the XRD spectra of the dephosphorized samples, confirming that the rare-earth phosphate had decomposed to its constituent oxides. The dephosphorized products were characterized by the presence of phases such as Ce₂O₃, CeO₂, Pr₂O₃, Nd₂O₃, and La₂O₃.

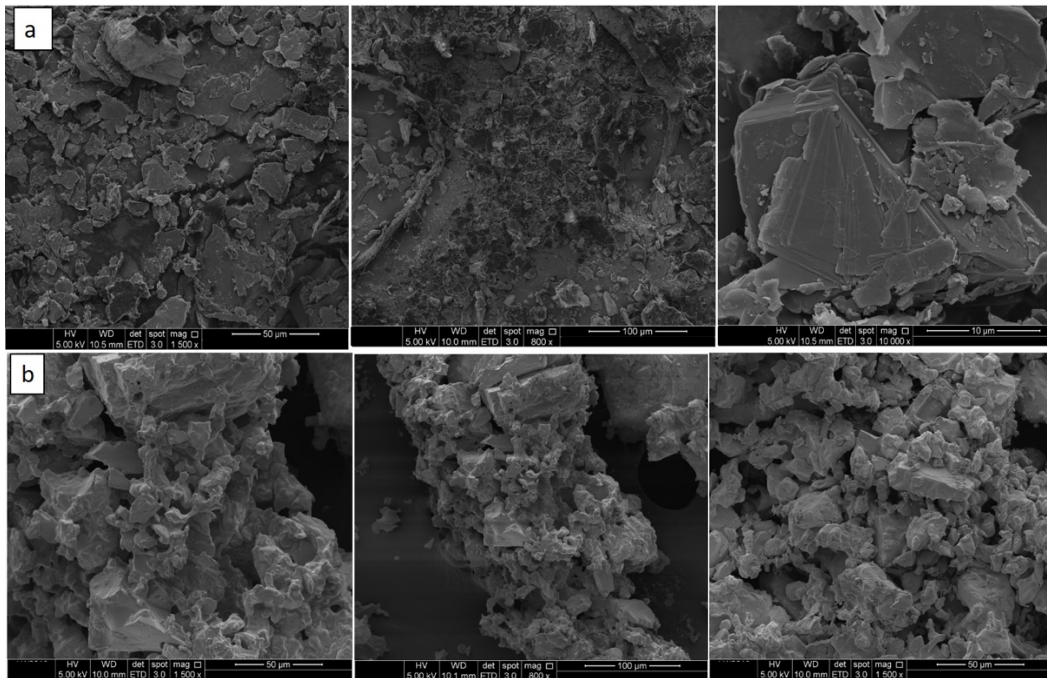


Fig.9. Secondary electron SEM images of a mixture of monazite concentrate and graphite; Sample HTD 8 (a) before and (b) after dephosphorization

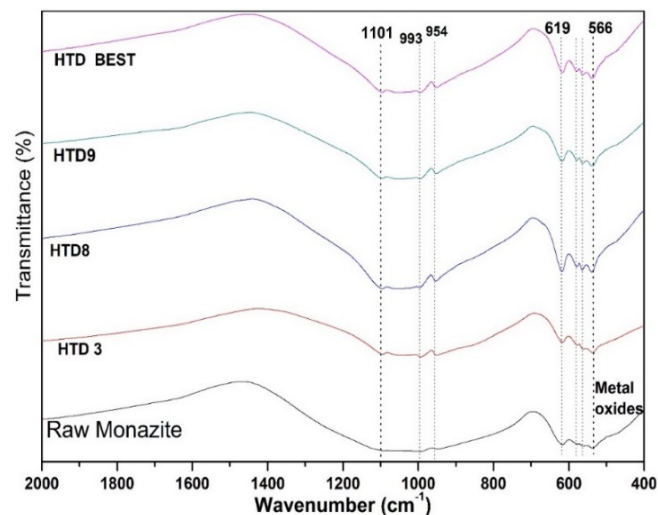


Fig. 10. Comparison of FTIR of dephosphorized products with raw monazite concentrate

5. Conclusions

The dephosphorization behavior of Malaysian monazite was studied using graphite as a reducing agent. Characterization of the raw concentrate revealed it contained 24.0-29.0 wt.% of phosphate (P_2O_5), 55.0-60.0 wt.% RE oxides, 5.0-10.0 wt.% thorium oxide (ThO_2) and 0.2-0.4 wt.% uranium oxide (U_3O_8). Modal analysis using EPMA of the concentrate confirmed that monazite was the dominant phase (96%), followed by zircon, xenotime, thorite, and cassiterite, which was also supported by quantitative XRD analysis. Thermodynamic analysis of monazite dephosphorization in air and in the presence of graphite indicated that reducing conditions promote decomposition at lower temperatures (1200 – 1350 °C) compared to air. A Taguchi experimental design approach was used to investigate the dephosphorization using graphite, and results showed a uniformly high degree of dephosphorization ($D_p > 97\%$). Detailed analysis of the results indicated that the reduction temperature was the most significant parameter, and the particle size was the least significant parameter. The extent of dephosphorization was 97.86% for optimal conditions consisting of a reducing temperature of 1350 °C,

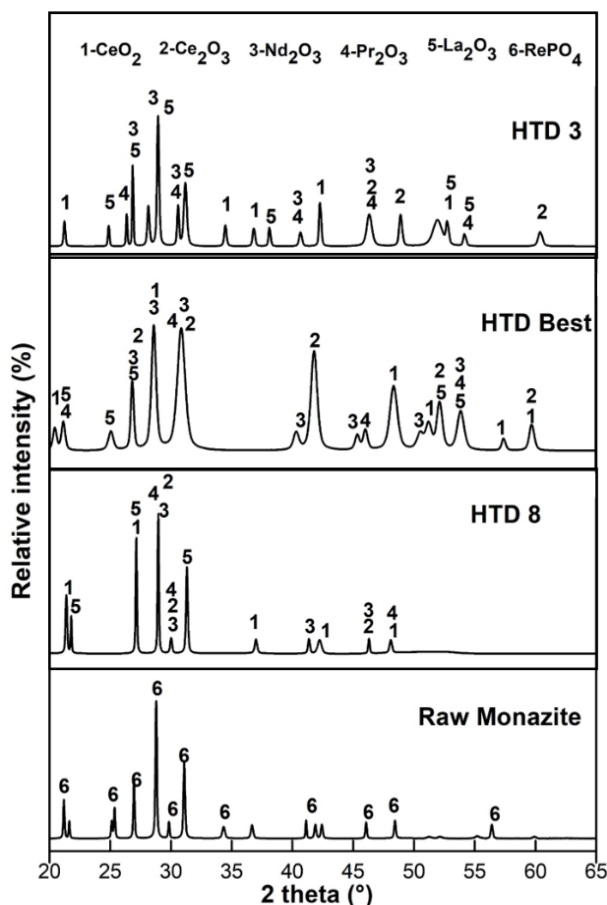


Fig. 11. Comparison of XRD patterns of selected dephosphorized samples with raw monazite concentrate

a molar ratio of monazite to graphite of 0.3, a particle size fraction of $-75\ \mu\text{m}$, and a run time of 2 h. Microstructural and phase characterization of the dephosphorized products showed that the dephosphorized products were in the form of a porous mass due to the removal of phosphorous. Phases of CeO_2 , Nd_2O_3 , La_2O_3 , and Pr_2O_3 were prominent, and no residual peaks of monazite were identified. FTIR studies of the dephosphorized products confirmed the removal of the phosphate group with the presence of dominant RE oxide bands. While the chosen parameters of size, monazite to carbon ratio, and temperature were essentially independent, the effect of time at that temperature on the extent of dephosphorization might be equally crucial. The rate kinetics of carbothermal dephosphorization could be investigated in future studies. However, based on the results of this study, the carbothermal dephosphorization method is a potential alternative processing route to produce RE oxides for subsequent leaching and recovery processes.

Acknowledgments

The authors wish to thank CSIRO Mineral Resources colleagues, Dr. Matthew Glenn, for assistance with scanning electron microscopy, Dr. Nathan Webster for quantitative XRD measurements, Dr. Nick Wilson for EPMA measurements, and Mr. Aaron Torpy for generating the EPMA map results. The authors express their gratitude to Mrs. Khaironie Mohamed Takip, Dr. Roshasnorlyza Hazan, Material Technology Group, Malaysian Nuclear Agency, and Dr. Teuku Andika Ramaputra, Prof. Dr. Ahmad Fauzi, School of Materials and Mineral Resources Engineering, USM for their supervision and technical advice. Special thanks to Mr. Abdul Mutalib Bin Abdullah, Mr. Khairul Anuar Safie, Earth Material Characterization Laboratory, Centre for Global Archeological Research, USM, and Mr. Mohammad Azrul and Mr. Mohamad Helmi Bin Khir, Mr. Shahrul Ami Bin Zainal Abidin, and Mr. Mohamad Shafiq Bin Mustapa Sukri in the School of Materials and Mineral Resources Engineering, USM.

The financial support from Universiti Sains Malaysia through USM Fellowship and Fundamental

Research Grant Schemes (FRGS Nos. 203/PBAHAN/6071364, Nos. 203/PBAHAN/6071402), and Bridging grant (304/PBAHAN/6316116) is acknowledged.

References

- ABREU, R. D., MORAIS, C. A. 2010. *Purification of rare earth elements from monazite sulphuric acid leach liquor and the production of high-purity ceric oxide*. Minerals Engineering, 23, 536-540.
- ARIFFIN, K. S. *Characteristics of processed ree-bearing heavy minerals associated with tin tailing from Kinta valley, Malaysia*. International Symposium on Earth Science and Technology, 2009. 237-242.
- BERRY, L., AGARWAL, V., GALVIN, J., SAFARZADEH, M. S. 2018. *Decomposition of monazite concentrate in sulphuric acid*. Canadian Metallurgical Quarterly, 57, 422-433.
- BERRY, L., GALVIN, J., AGARWAL, V., SAFARZADEH, M. 2017. *Alkali pug bake process for the decomposition of monazite concentrates*. Minerals Engineering, 109, 32-41.
- COTTRELL, T. 1958. *Other measures of bond strength*. The Strengths of Chemical Bonds, 2, 260-289.
- FRANKEN, K. 1995. *A roast-leach process for extraction of rare earths from complex monazite-xenotime concentrates*. Separation Science and Technology, 30, 1941-1949.
- GUPTA, C., MUKHERJEE, T. 1990. *Hydrometallurgy in extraction processes*, CRC Press.
- HA, Y. G. 1979. *Decomposition of monazite sand*. Journal of the Korean Chemical Society, 23, 136-140.
- HARROWFIELD, I., MACRAE, C., WILSON, N. 1993. *Proceedings of the 27th annual mas meeting 1993*.
- HUANG, Y., ZHANG, T. A., JIANG, L., ZHIHE, D., JUNHANG, T. 2016. *Decomposition of the mixed rare earth concentrate by microwave-assisted method*. Journal of Rare Earths, 34, 529-535.
- KARSHIGINA, Z., ABISHEVA, Z., BOCHEVSKAYA, Y., AKCIL, A., SARGELOVA, E., SUKUROV, B., SILACHYOV, I. 2018. *Recovery of rare earth metals (rems) from primary raw material: Sulphatization-leaching-precipitation-extraction*. Mineral Processing and Extractive Metallurgy Review, 39, 319-338.
- KEEKAN, K. K., JALONDHARA, J. C., ABHILASH 2017. *Extraction of ce and th from monazite using ree tolerant aspergillus niger*. Mineral Processing and Extractive Metallurgy Review, 38, 312-320.
- KEMP, D. 2017. *The feasibility of extraction of thorium and rare earths from monazite through a thermal plasma and a chemical treatment process*. North-West University (South Africa), Potchefstroom Campus.
- KEMP, D., CILLIERS, A. 2016. *High-temperature thermal plasma treatment of monazite followed by aqueous digestion*. Journal of the Southern African Institute of Mining and Metallurgy, 116, 901-906.
- KIM, W., BAE, I., CHAE, S., SHIN, H. 2009. *Mechanochemical decomposition of monazite to assist the extraction of rare earth elements*. Journal of Alloys and compounds, 486, 610-614.
- KRISHNAMURTHY, N., GUPTA, C. K. 2015. *Extractive metallurgy of rare earths*, CRC press.
- KUMARI, A., PANDA, R., JHA, M. K., KUMAR, J. R., LEE, J. Y. 2015. *Process development to recover rare earth metals from monazite mineral: A review*. Minerals Engineering, 79, 102-115.
- MERRITT, R. R. 1990a. *High temperature methods for processing monazite: I. Reaction with calcium chloride and calcium carbonate*. Journal of the Less Common Metals, 166, 197-210.
- MERRITT, R. R. 1990b. *High temperature methods for processing monazite: li. Reaction with sodium carbonate*. Journal of the Less Common Metals, 166, 211-219.
- NI, Y., HUGHES, J. M., MARIANO, A. N. 1995. *Crystal chemistry of the monazite and xenotime structures*. American Mineralogist, 80, 21-26.
- NRIAGU, J. O. 1984. *Phosphate minerals: Their properties and general modes of occurrence*. Phosphate minerals. Springer.
- PENGFELI, X., FENG, L., JING, G., TU, G. 2010. *High temperature dephosphorus behavior of baotou mixed rare earth concentrate with carbon*. Journal of rare earths, 28, 194-197.
- ROINE, A., MANSIKKA-AHO, J., BJÖRKLUND, P., KENTALA, J.-P., TALONEN, T. 2006. *Outokumpu hsc chemistry, chemical reaction and equilibrium software with extensive thermochemical database*. Finland: Outokumpu.
- SADRI, F., NAZARI, A. M., GHahreman, A. 2017. *A review on the cracking, baking and leaching processes of rare earth element concentrates*. Journal of Rare Earths, 35, 739-752.
- SHEIBLEY, D. W., FOWLER, M. H. 1966. *Infrared spectra of various metal oxides in the region of 2 to 26 microns*. National Aeronautics and Space Administration, Cleveland, Ohio. Lewis Research Center.
- SUÁREZ-RUIZ, I., CRELLING, J. C. 2008. *Coal-derived carbon materials*. Applied coal petrology. Elsevier.
- TAGUCHI, G. 1986. *Introduction to quality engineering: Designing quality into products and processes*.
- TRIPATHY, M., RANGANATHAN, S.H MEHROTRA, S. 2012. *Investigations on reduction of ilmenite ore with different sources of carbon*. Mineral Processing and Extractive Metallurgy, 121, 147-155.

- UDAYAKUMAR, S., NOOR, A. F. M., HAMID, S. A. R. S. A., PUTRA, T. A. R., ANDERSON, C. G. 2020. *Chemical and mineralogical characterization of malaysian monazite concentrate*. *Mining, Metallurgy, Exploration*, 1-17.
- WANG, Y., YUAN, Z. 2006. *Reductive kinetics of the reaction between a natural ilmenite and carbon*. *International journal of mineral processing*, 81, 133-140.
- WILSON, N., MACRAE, C. 2005. *An automated hybrid clustering technique applied to spectral data sets*. *Microscopy and Microanalysis*, 11, 434-435.
- XING, P.-F., ZHUANG, Y.-X., TU, G.-F., JING, G. 2010. *High temperature dephosphorization behavior of monazite concentrate with charred coal*. *Transactions of Nonferrous Metals Society of China*, 20, 2392-2396.
- YUAN, S., YANG, H., XUE, X.-X., ZHOU, Y. 2017. *Kinetics of roasting decomposition of the rare earth elements by cao and coal*. *Metals*, 7, 213.
- ZHANG, J.-P., LINCOLN, F. J. 1994. *The decomposition of monazite by mechanical milling with calcium oxide and calcium chloride*. *Journal of alloys and compounds*, 205, 69-75.
- ZHENG, Q., BIAN, X., WU, W.-Y. 2017a. *An environmental friendly coal-ca (oh) 2-naoh roasting decomposition strategy for bayan obo tailings*. *Metallurgical Research, Technology*, 114, 201.
- ZHENG, Q., WENYUAN, W., XUE, B. 2017b. *Investigations on mineralogical characteristics of rare earth minerals in bayan obo tailings during the roasting process*. *Journal of Rare Earths*, 35, 300-308.